Ab Initio Structures and Energetics of Hydrated Flat and Terrace-Step Surfaces of Forsterite (Mg_2SiO_4)

Duo Song[a*], Sebastien N. Kerisit[a], John S. Loring[a*]

[a] Physical & Computational Sciences Directorate, Pacific Northwest National Laboratory, Richland, Washington 99354, USA

[*] Corresponding Authors: duo.song@pnnl.gov and john.loring@pnnl.gov

Abstract

Forsterite (Mg_2SiO_4), a model divalent metal silicate mineral, has been extensively studied in the context of mineral carbonation. Although dissolution is a key step in this process, the mechanisms by which forsterite dissolves under high CO_2 conditions remain poorly understood. Atomistic simulations could aid in exploring these mechanisms, but it is essential first to understand the structures and energetics of the relevant forsterite surfaces. We present an ab initio study of the structure and surface energy at 0 K of the flat (010), (110), (001), (111), (021), (101) and (120) faces of forsterite using the density functional PBE Hamiltonian and a plane-wave basis set. Dry surfaces became stabilized upon hydration through the formation of bonds between surface Mg and O from water, as well as by the formation of hydrogen bonds. According to surface energy values, the stability order of the hydrated forsterite faces was found to be (120) < (101) < (021) < (111) < (001) < (110) < (010). We also investigated the energetics of the terrace-step $(0\bar{4}1)$ surface as a model site for forsterite dissolution. Among all the facets, the $(0\bar{4}1)$ surface is the least stable termination in water. Hydration of Mg atoms on the $(0\bar{4}1)$ surface increases their susceptibility to dissolution. The presence of a step and its hydration destabilizes the terraces, making step retreat more likely than a dissolution front advancing along the [010] direction. This research will support future simulations to investigate forsterite dissolution in water under CO_2-rich conditions.

Introduction

Olivine (M_2SiO_4; M=Mg, Fe) is a common mineral found in (ultra)mafic rocks, consisting of isolated silicate tetrahedra connected to metal octahedra through oxygen bonds. Due to its high divalent cation content and reactivity, olivine carbonation has attracted significant interest as a method for sequestering anthropogenic carbon dioxide to help mitigate global warming.[1-4]

The Mg-endmember of olivine, forsterite (Mg_2SiO_4), has been the focus of numerous experimental[5-17] and computational[18-21] studies on the carbonation of divalent metal silicates. During forsterite carbonation, CO_2 reacts with water to form carbonic acid, leading to the dissolution of forsterite and the precipitation of magnesium carbonates. Dissolution is a key step in this process, yet the mechanisms by which it occurs under high CO_2 conditions remain unclear. In the absence of CO_2, protonation of oxygens in Si-O-Mg linkages causes Mg-O bond rupture, followed by nucleophilic attack by water, releasing a fully hydrated Mg^{2+}. However, experiments conducted in CO_2-rich environments have shown the formation of bicarbonate complexes on the forsterite surface.[9] In such cases, Mg-coordinated bicarbonate anions may weaken the Mg-O bonds to the forsterite sublattice, making them more susceptible to proton-induced rupture and potentially accelerating Mg^{2+} dissolution. Understanding the dominant mechanism of forsterite dissolution under CO_2-rich conditions is crucial for developing effective strategies to store carbon dioxide durably, but current experiments cannot definitively determine whether the primary mechanism is proton or bicarbonate-promoted.

Atomistic simulations would be useful for explore the dissolution mechanisms of forsterite under CO_2-rich conditions. However, it is essential to first understand the structures and energetics of the relevant forsterite surfaces. Forsterite surfaces have been the focus of several previous

computational studies.[18-33] For dry forsterite, recent density functional theory (DFT) studies by Bruno et al. and Demichelis et al. calculated the surface energies of the (010), (101), (111), (001), (110), (120), and (021) faces.[31, 33] They showed that the (010) face is the most stable under dry conditions and explained the shape of olivine inclusions in diamond.[31] For hydrated forsterite, De Leeuw et al. used atomistic simulations with empirical potentials to calculate the hydrated surface energies of the (001), (010), (100), (011), (101), (110), (111), and (021) faces and correctly predicted the morphology of forsterite equilibrated in water.[28] King et al. employed similar methods to demonstrate that dissociative water adsorption is favored at steps, corner sites, and vacancies on the (001), (010), (100), (110), and (101) faces. They concluded that water retention is possible even at low partial pressures and high temperatures at these low-coordinated surface sites.[29] To our knowledge, only a few studies have used ab initio level calculations to investigate hydrated forsterite surfaces. Kerisit et al. calculated water and carbon dioxide adsorption energies on the (010) surface using DFT and showed that carbon dioxide is easily displaced by water at the (010) surface to form thin water films in which dissolution and carbonate precipitation can take place.[18, 19] Asaduzzaman et al. used DFT calculations to show that water dissociation followed adsorption on the (001), (100), (010) and (110) faces of forsterite, although two stable associative adsorption configurations were also identified.[27]

A comprehensive study of hydrated forsterite flat surfaces using ab initio calculations is still lacking. Additionally, to our knowledge, no ab initio studies have been conducted on dry or hydrated forsterite step surfaces. This article aims to investigate the structures and energetics of the crystal faces and a specific terrace-step surface of forsterite using DFT calculations and two-dimensional slab models. We initially focused on flat surfaces to establish a baseline for step energy calculations. Inspired by previous DFT studies by Bruno et al. and Demichelis et al. on

dry surfaces[31, 33], we determined the equilibrium geometries and surface energies at 0 K for the hydrated (010), (101), (111), (001), (110), (120), and (021) faces of forsterite. This approach allowed us to establish a robust baseline and align our findings with existing literature. Subsequently, we concentrated on a terrace-step surface featuring two types of Mg terminations, as recent studies by Li et al. using atomic force microscopy have suggested that forsterite step surfaces are the primary sites for forsterite dissolution.[34-36] The research presented here will be beneficial for future simulations of dissolution at forsterite/water interfaces under CO_2-rich conditions, helping to determine whether the primary mechanism of forsterite dissolution is promoted by protons or bicarbonate.

Computational Methods

All geometry optimizations and surface energies of forsterite crystal facets in this study were performed using DFT[37] with the pseudopotential plane-wave NWPW module[38] implemented in the NWChem software package[39, 40]. The generalized gradient approximation of Perdew-Burke-Ernzerhof (PBE)[41] was used to account for the exchange-correlation energy. In our plane-wave calculations, the valence electron interactions with the atomic core were approximated with generalized norm-conserving Hamann pseudopotentials[42, 43] for Si, O, and H. Norm-conserving Troullier-Martins pseudopotentials[44], which contain 4s, 4p, and 3d projectors and a semi-core correction, were applied for Mg. All the pseudopotentials were modified to the separable form suggested by Kleinman and Bylander[45]. Spin-restricted calculations were performed since the hydrated forsterite crystal facets are closed-shell systems. The structural properties of a perfect bulk forsterite crystal were first optimized using a 2×1×2 Monkhorst-Pack Brillouin zone sampling. For the slabs, the electronic wavefunctions were expanded using a plane-wave basis

with periodic boundary conditions at the Γ-point (1×1×1 *k*-point mesh) with a wavefunction cutoff energy of 100 Ry and a density cutoff energy of 200 Ry. All atomic positions were entirely relaxed using the default NWChem DRIVER optimizer until the forces on the atoms were converged to less than 10^{-4} hartree/bohr and the total energy was converged to less than 10^{-6} hartree.

The specific surface energy γ_{hkl} (J/m^2) of a dry crystal face hkl at a temperature of T = 0 K was calculated as[46]

$$\gamma_{hkl} = \frac{E_{hkl}^{n,0} - n \times E_{\text{bulk}}^{\text{Mg}_2\text{SiO}_4}}{2A}$$

where $E_{hkl}^{n,0}$ is the energy of a dry forsterite slab of crystal face hkl with n Mg_2SiO_4 stoichiometric units, $E_{\text{bulk}}^{\text{Mg}_2\text{SO}_4}$ is the bulk energy per stoichiometric unit, A is the surface area, and the factor of 2 in the denominator accounts for the upper and lower surfaces of the slab model.

The surface energy of a hydrated crystal face hkl, γ_{hkl} (J/m^2) was defined as

$$\gamma_{hkl} = \frac{E_{hkl}^{n,m} - n \times E_{\text{bulk}}^{\text{Mg}_2\text{SO}_4} - m \times E_{\text{bulk}}^{\text{ice XI}}}{2A}$$

where $E_{hkl}^{n,m}$ is the energy of a hydrated forsterite slab of crystal face hkl with n Mg_2SiO_4 stoichiometric units and m adsorbed water molecules, and $E_{\text{bulk}}^{\text{ice XI}}$ is the bulk energy of ice XI per H_2O molecule. Because the calculations in this study did not consider temperature, ice was selected as the reference phase for H_2O instead of liquid water. Ice XI, the hydrogen-ordered form of ordinary ice, is the equilibrium structure below approximately 70 K at ambient pressure.

The lattice parameters of Ice XI are presented in Table S1 and compared with those obtained by Leadbetter et al.[47] at 5 K from neutron powder diffraction data.

The adsorption energy of water on the forsterite facet hkl, $\Delta E_{\mathrm{H_2O}}^{hkl}$,was defined as

$$\Delta E_{\mathrm{H_2O}}^{hkl} = \frac{E_{hkl}^{n,m} - E_{hkl}^{n,0} - m \times E_{\mathrm{gp}}^{\mathrm{H_2O}}}{m}$$

where $E_{\mathrm{gp}}^{\mathrm{H_2O}}$ is the energy of a water molecule in the gas phase.

The step energy, ξ (J/m), of the terrace-step surface was determined by[48]

$$\xi = d\left(\frac{\gamma^* A^*}{A} - \gamma\right)$$

where γ^* represents the specific surface energy for the terrace-step face, A^* is the area of the vicinal surface enclosed within the simulation cell, γ represents the surface energy of the cleavage surface in the simulation cell, A is the area of this cleavage surface, and d is the step separation.

Structures and Energetics of Low-Index, Flat Forsterite Surfaces

The forsterite crystal structure was first optimized, which yielded the lattice parameters *a* = 4.7188 Å (−0.6%), *b* = 10.0549 Å (−1.4%), *c* = 5.9073 Å (−1.2%) where the percentage differences relative to the experimental lattice parameters (*a* = 4.7490 Å, *b* = 10.1985 Å, *c* = 5.9792 Å[49], Pbnm space group) are shown in parentheses. The optimized crystal structure was then cut using METADISE[50] to generate seven low-index surfaces, namely, (010), (110), (001), (111), (021), (101) and (120). These surfaces are the same as those considered by Bruno et al.[31]

and constitute the most comprehensive set of surfaces studied to date with electronic structure methods. The two-dimensional cell parameters of the slabs are listed in Table S2 All slabs contained 224 atoms, i.e., 64 Mg atoms, 32 Si atoms, and 128 O atoms.

Hydrated forsterite surfaces were generated by adsorbing a monolayer of water molecules to the dry forsterite surfaces, with the number of water molecules determined to ensure that all Mg atoms that were undercoordinated as a result of the surface formation regained six-fold coordination. Water was initially adsorbed associatively, i.e., as a molecule, in all cases. During energy minimization of the hydrated surfaces, a fraction of the adsorbed water molecules spontaneously dissociated into H^+ and OH^- on all the surfaces except (010) and (120) (Table 1). The as-cleaved, relaxed dry, and relaxed hydrated structures of the seven surfaces are shown in Figure 1.

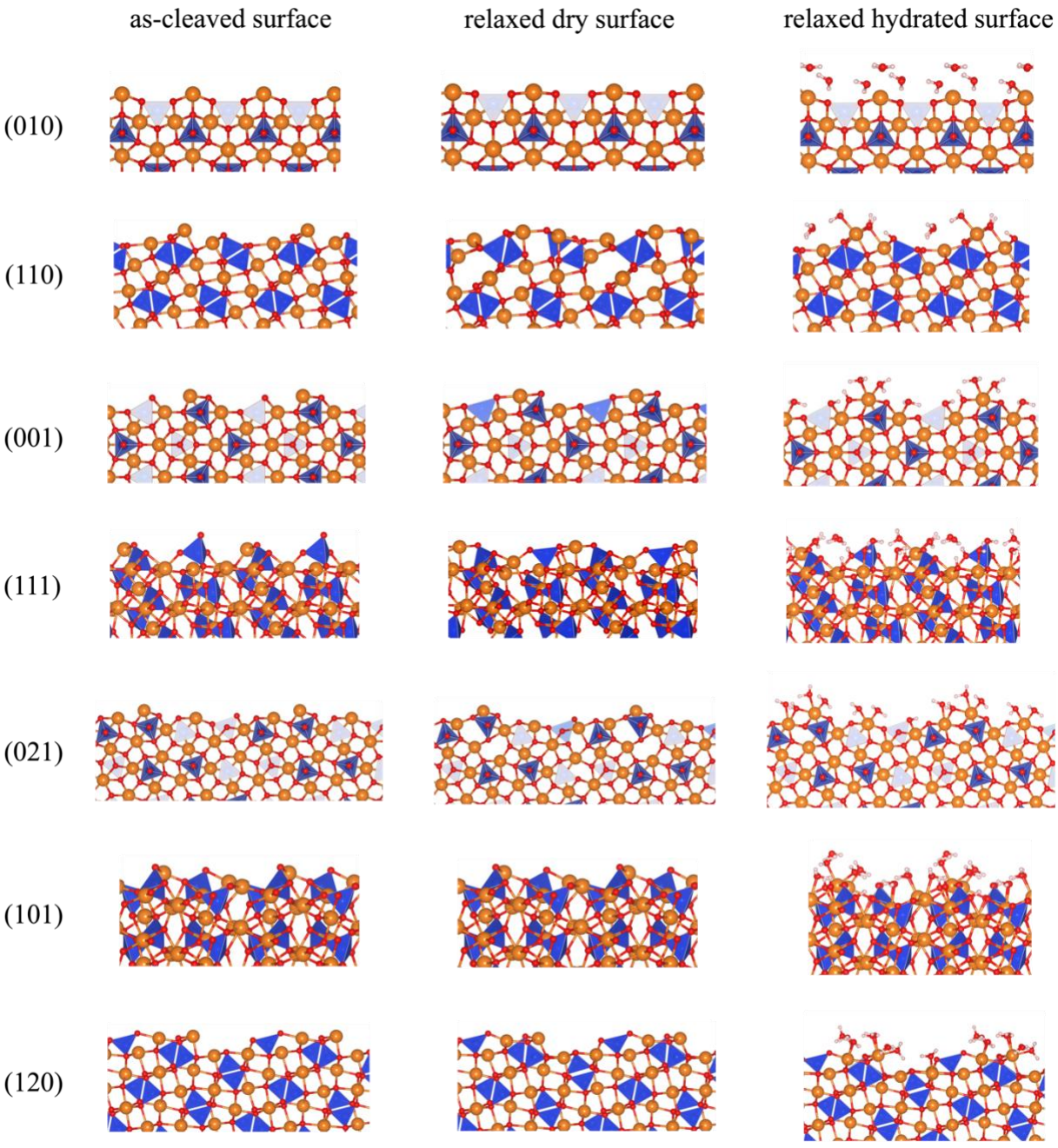

Figure 1. Combined polyhedral and ball-and-stick models of the (010), (110), (001), (111), (021), (101), and (120) surfaces of forsterite (Mg_2SiO_4). For each facet, the as-cleaved, relaxed dry, and relaxed hydrated structures are displayed from left to right. SiO_4 tetrahedra are shown in blue and Mg, O, and H atoms are shown as orange, red, and white balls, respectively.

Table 1. Numbers of Adsorbed Water Molecules and Dissociated Water Molecules of Hydrated Forsterite (010), (110), (001), (111), (021), (101), and (120) Surfaces.

Face	Total number of adsorbed water molecules	Number of dissociated water molecules
(**010**)	24	0
(**110**)	24	8
(**001**)	16	4
(**111**)	28	4
(**021**)	24	4
(**101**)	24	4
(**120**)	24	0

Table 2 lists the surface energies as well as the water adsorption energies of the seven dry and hydrated forsterite surfaces considered in this work, and Table 3 compares the surface energies of the seven dry forsterite faces calculated here to values reported in the literature. From Table 2, the dry surfaces, from lowest to highest surface energies (i.e., from most to least stable), were (010) < (120) < (001) < (101) < (111) < (021) < (110). This order of stability matches exactly that reported by Bruno et al.[31] (Table 3) based on DFT calculations performed with an all-electron, Gaussian-type basis set and the B3LYP exchange-correlation approximation. Zamirri et al.[26] reported a similar order of stability (with only the (101) and (001) surfaces swapped) computed at the B3LYP//B3LYP-D* (in parentheses) level, where single-point energies at the B3LYP level were calculated using the geometries optimized with B3LYP-D* and the same Gaussian-type basis set as employed by Bruno et al. Figure 2 shows that, although the surface

energies obtained in this work for dry surfaces were systematically lower than those reported by Bruno et al. and Zamirri et al., they were highly correlated. In contrast, surface energies obtained with PBE and the pob-TZVP basis set by Demichelis et al.[33] exhibited exactly the same order of stability and similar values (with differences of at most 6%) as obtained in this work (Table 3 and Figure 2). The orders of stability obtained by de Leeuw et al.[28] and Watson et al.[30] using empirical potentials were the same as calculated here, except for the (101) and (111) surfaces being swapped. However, the surface energies were systematically higher than those obtained here with DFT (Figure 2). This difference is line with expectations because the DFT calculations account for electronic degrees of freedom that are not explicitly treated in calculations based on empirical potentials.

Table 2. Surface Energies, γ (J/m^2), at 0 K and Adsorption Energies, $\Delta E^{hkl}_{H_2O}$ (kJ/mol), of the Hydrated and Dry Surfaces of Forsterite.

Face	Hydrated	Dry	$\Delta E^{hkl}_{H_2O}$
(**010**)	0.53	0.99	-80.6
(**110**)	0.55	1.80	-137.2
(**001**)	0.57	1.33	-127.2
(**111**)	0.59	1.43	-124.7
(**021**)	0.60	1.50	-134.4
(**101**)	0.66	1.36	-108.5
(**120**)	0.70	1.04	-83.2

Table 3. Comparison of the Surface Energies, γ (J/m^2), Obtained in this Work at 0 K for the Seven Dry Forsterite Faces to Literature Data.

Face	This work	Bruno et al.[31]	De Leeuw et al.[28]	Watson et al.[30]	Zamirri et al.[26]	Demichelis et al.[33] (PBE)
(**010**)	0.99	1.22	1.28	1.28	1.44 (1.23)	0.94
(**110**)	1.80	2.18	1.96	2.28	2.46 (2.17)	1.71
(**001**)	1.33	1.78	1.74	1.61	1.98 (1.72)	1.29
(**111**)	1.43	1.84	1.81	1.80	2.19 (1.83)	1.35
(**021**)	1.50	1.90	1.94	1.95	2.24 (1.91)	1.41
(**101**)	1.36	1.78	1.88	1.81	1.96 (1.62)	1.30
(**120**)	1.04	1.36	1.56	1.56	1.68 (1.37)	1.09

The order of adsorption energies (from least to most exothermic) was (120) < (010) < (101) < (111) < (001) < (021) < (110), which agreed with the order (010) < (001) < (110) obtained by Asaduzzaman et al.[27, 32] using DFT PBE with the PAW method (Table 4). Comparing this order to the order of stability of the dry surfaces above indicated that the high-energy dry surfaces generally had the largest adsorption energies and were thus stabilized the most upon hydration. As a result, the hydrated surfaces from lowest to highest surface energies were (010) < (110) < (001) < (111) < (021) < (101) < (120). Although the water adsorption energy on the (010) surface was one of the least exothermic adsorption energies, this surface remained the most stable surface. Furthermore, the surface energies of the hydrated surfaces were not correlated to

the dry surface energies (Figure 2), indicating that the forsterite surfaces were stabilized to different extents by water adsorption.

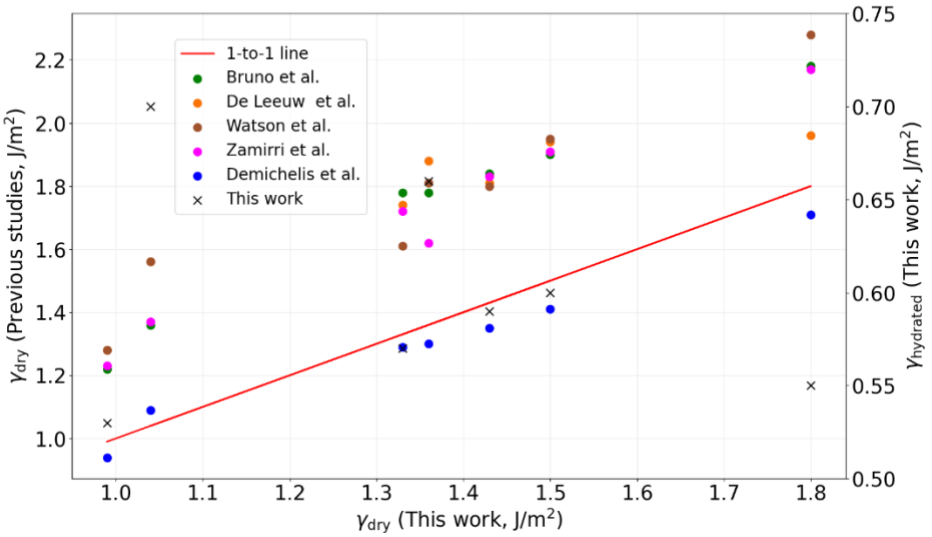

Figure 2. Correlations between literature and calculated surface energies of the dry forsterite surfaces and between surface energies of the hydrated (black ×) and dry forsterite surfaces calculated in this work.

Table 4. Comparison of the Adsorption Energies (kJ/mol) of the Forsterite Crystal Faces (010), (001) and (110) from This Work and Previous Studies

Face	This work	Asaduzzaman et al.[27, 32]
(010)	-80.6	-91.7
(001)	-127.2	-169.8
(110)	-137.2	-183.3

To correlate the calculated adsorption energies to the hydrated surface structures, the total number and density per unit of surface area of hydrogen bonds, total number and density per unit of surface area of Mg–O bonds broken upon cleaving, and total number and density per unit of surface area of Mg–O_w bonds (between Mg and O from water) formed upon hydration were calculated and are presented in Table 5. We identified hydrogen bonds based on the following structural and geometric criteria.[51] The H···O_A (hydrogen to acceptor oxygen) distance is between 1.5 and 2.5 Å, while the O_D···O_A (donor oxygen to acceptor oxygen) distance is within 2.6 to 3.5 Å. Additionally, the O_D–H···O_A bond angle should be greater than 120°. The order of density of hydrogen bonds per unit of surface area was (120) < (010) < (101) < (111) < (001) < (021) < (110), which matched exactly the order of adsorption energies. A high hydrogen bond density enhanced the stability of the hydrated surface by providing cohesive forces and thus reducing the surface energy. Besides, the order of density of Mg–O_w bonds formed upon hydration was (120) < (101) < (021) < (001) < (010) < (111) < (110). Comparing this order to that of the adsorption energies indicated that the formation of Mg–O_w bonds contributed to stabilizing the dry surfaces. For example, the surface energy of the (110) surface, the most unstable dry surface, decreased from 1.80 J/m^2 to 0.55 J/m^2 upon hydration due to the most exothermic adsorption energy of −137.2 kJ/mol, which, in turn, was due to the highest hydrogen bond density of 0.122 $Å^{-2}$ and the highest density of Mg–O_w bonds of 0.137 $Å^{-2}$. Figure 1 illustrates that some water molecules adsorbed within the gaps of the (110) surface, which effectively smoothed the surface topography. Conversely, while the (120) surface had the second lowest dry surface energy, it became the least stable surface upon hydration due to an adsorption energy of only −83.2 kJ/mol because its hydration structure resulted in the lowest hydrogen bond density (0.080 $Å^{-2}$) and the lowest density of Mg–O_w bonds (0.086 $Å^{-2}$). In addition, water

molecules clustered around Mg ions, increasing the surface roughness. These findings are consistent with previous studies on hydration of minerals such as MgO[52], Al_2O_3[53], and $CaCO_3$[54], which showed significant stabilization of otherwise relatively unstable surfaces.

Table 5. Surface Areas, Total Number of Hydrogen Bonds ($N_{\mathrm{H-bond}}$), Density of Hydrogen Bonds per Unit of Surface Area ($D_{\mathrm{H-bond}}$), Number of Mg–O Bonds Broken upon Cleaving ($N_{\mathrm{Mg-O}}^{\mathrm{broken}}$), Density of Mg–O Bonds Broken upon Cleaving ($D_{\mathrm{Mg-O}}^{\mathrm{broken}}$), Number of Mg–$O_w$ Bonds Formed upon Hydration ($N_{\mathrm{Mg-O_w}}^{\mathrm{formed}}$), and Density of Mg–$O_w$ Bonds Formed upon Hydration ($D_{\mathrm{Mg-O_w}}^{\mathrm{formed}}$) on Hydrated Surfaces of Forsterite.

Face	Surface area ($Å^2$)	$N_{\mathrm{H-bond}}$	$D_{\mathrm{H-bond}}$ ($Å^{-2}$)	$N_{\mathrm{Mg-O}}^{\mathrm{broken}}$	$D_{\mathrm{Mg-O}}^{\mathrm{broken}}$ ($Å^{-2}$)	$N_{\mathrm{Mg-O_w}}^{\mathrm{formed}}$	$D_{\mathrm{Mg-O_w}}^{\mathrm{formed}}$ ($Å^{-2}$)
(**010**)	111.50	19	0.085	24	0.108	24	0.108
(**110**)	131.23	32	0.122	36	0.137	36	0.137
(**001**)	94.89	20	0.105	20	0.105	20	0.105
(**111**)	161.94	32	0.099	44	0.136	36	0.111
(**021**)	146.42	31	0.106	30	0.102	30	0.102
(**101**)	152.04	26	0.086	40	0.132	30	0.099
(**120**)	162.93	26	0.080	32	0.098	28	0.086

Structure and Energetics of a Terrace-Step Forsterite Surface

At the atomic-level, mineral dissolution typically occurs via step retreat. Therefore, we set out to identify a candidate step surface for simulating forsterite dissolution. Because the (010) surface was identified above as the most stable forsterite surface, in both dry and hydrated conditions,

we generated a terrace-step surface whose terrace consisted of the (010) surface, as depicted in Figure 3. The step spacing was limited by the size of the simulation cell that can be reasonable treated with the level of theory used in this work. The resulting terrace-step surface was the $(0\bar{4}1)$ surface (Figure 3). There are two symmetry-inequivalent Mg sites in forsterite denoted M1 and M2. Planes of M1 and M2 sites alternate along the [010] direction. Only the cleavage plane that exposes the plane of M2 sites at the (010) surface produces a non-polar surface that leaves the SiO_4 tetrahedra intact. Therefore, the two terraces of the $(0\bar{4}1)$ surface are terminated by M2 sites. The dry $(0\bar{4}1)$ slab was charge-neutral and contained 224 atoms including 64 Mg atoms, 32 Si atoms, and 128 O atoms. 64 water molecules were added to generate the hydrated surface, 10 of which spontaneously dissociated during the energy minimization. The optimized average Si−O distances at the dry and hydrated $(0\bar{4}1)$ surfaces were 1.642 Å and 1.639 Å, respectively. The Mg atoms at the step edge were undercoordinated with only 5 oxygen ligands (3 from water molecules and 2 from silicate oxygen atoms), implying that these step-edge Mg atoms were less stable compared to other surface Mg atoms. Our terrace-step surface closely resembles the small-stepped (010) surface proposed by King et al.,[29] except that their model included two additional outer layers of SiO_4 tetrahedra and Mg atoms above our outmost M2-type Mg layer, while our structure has an extra layer of M1-type Mg atoms below the outmost M2-type Mg layer.

The surface energies of the dry and hydrated terrace-step surfaces were calculated to be 1.30 J/m^2 and 1.03 J/m^2, respectively, and the water adsorption energy was -67.1 kJ/mol^{-1}. The surface energy of the hydrated $(0\bar{4}1)$ surface was higher than any of the flat surfaces, indicating it is the most unstable surface in water. The step energy for the dry $(0\bar{4}1)$ surface was calculated to be 1.05×10^{-9} J/m, while for the hydrated surface it was 0.92×10^{-9} J/m. This result indicates that the formation of steps is energetically more favorable in the hydrated state due to water

molecules reducing surface energy and stabilizing step edges. On the hydrated $(0\bar{4}1)$ surface, the surface Mg atoms are six-fold coordinated with four water molecules and two silicate oxygen atoms. In contrast, on the hydrated (010) surface, the surface Mg atoms are also six-fold coordinated but are bonded to three water molecules and three silicate oxygen atoms. The greater number of water molecules bonded to the Mg atoms on the $(0\bar{4}1)$ surface makes them more susceptible to preferential dissolution. This difference suggests that the presence of a step and its hydration disrupt the terraces, making step retreat far more likely than a dissolution front advancing along the [010] direction. This dissolution behavior is consistent with atomic force microscopy (AFM) observations of (010) surface dissolution through etch-pit expansion[34-36]. Moreover, the step heights of the dry and hydrated step surface were calculated to be 0.57 nm and 0.54 nm, respectively, which closely matched the average height (0.58 ± 0.07 nm) of the steps around pits measured by Li et al.[34] using AFM. This agreement indicates that the $(0\bar{4}1)$ terrace-step surface is a plausible model for the atomic structure of observed etch-pit walls.

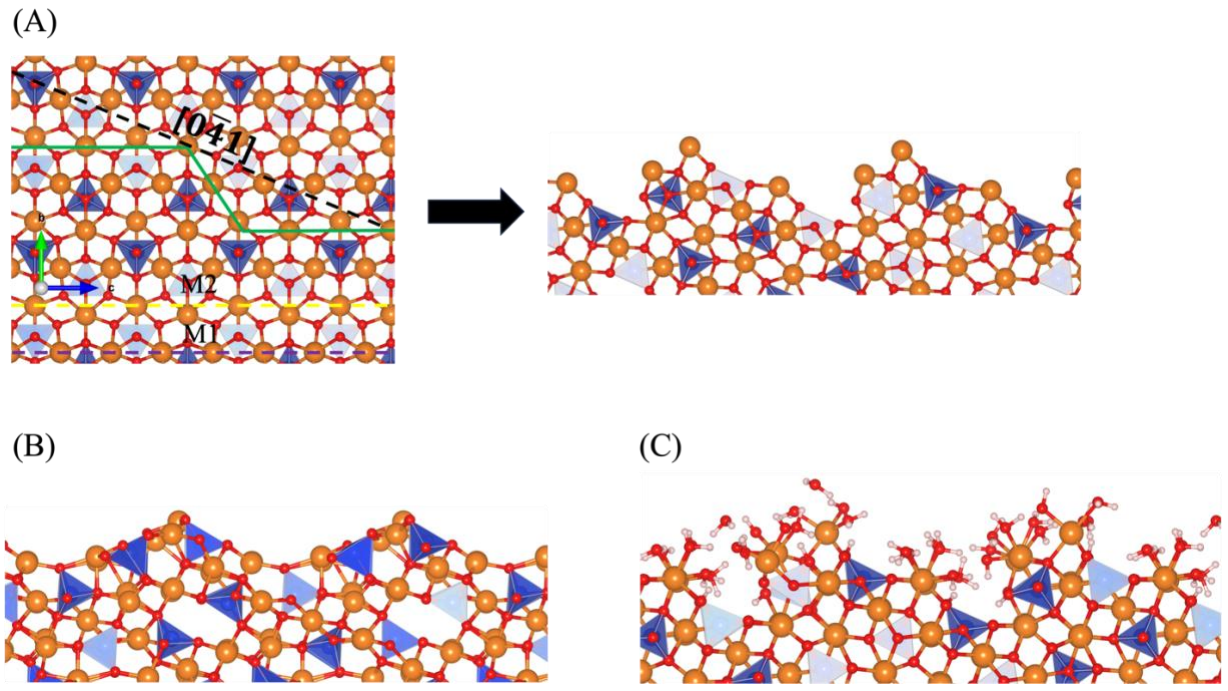

Figure 3. (A) Step surface cleavage along the $[0\bar{4}1]$ direction is indicated by the black dashed line. The M1 and M2 terminations are represented by the purple and yellow dashed lines, respectively. The green line outlines the terrace and step on the $(0\bar{4}1)$ surface. The as-cleaved $(0\bar{4}1)$ surface is shown in the right. (B) The relaxed dry $(0\bar{4}1)$ surface. (C) The relaxed hydrated $(0\bar{4}1)$ surface. SiO_4 tetrahedra are shown in blue and Mg, O, and H atoms are shown as orange, red, and white balls, respectively.

Conclusions

The structures and surface energies at 0 K of the dry and hydrated (010), (110), (001), (111), (021), (101) and (120) forsterite faces have been calculated using the PBE Hamiltonian and a plane-wave basis set. The stability order (the reverse of the surface energy order) of the hydrated forsterite faces is (120) < (101) < (021) < (111) < (001) < (110) < (010). All surfaces readily adsorb water, with adsorption energies ranging from −80 to −140 kJ/mol. Major contributions to the adsorption energies were from the formation of $Mg–O_w$ bonds and hydrogen bonds between lattice oxygens and other water molecules. Dissociative adsorption of water is energetically favorable on most surfaces. The (120) facet is the least stable surface termination in water due to its low water adsorption energy.

The $(0\bar{4}1)$ terrace-step has the least favorable hydrated surface energy compared to the flat surfaces. Its step energy, which is useful for studying the energetics required to generate an active surface for the dissolution, was found to be 1.05×10^{-9} J/m for the dry surface and 0.92×10^{-9} J/m for the hydrated surface. This implies that step formation is energetically more favorable on the hydrated surface. Upon hydration, the surface Mg atoms are bonded with more water molecules than those on (010) facet, suggesting that dissolution of Mg atoms is probable on this

surface. This difference indicates that the presence of a step and its hydration disrupt the terraces, which makes step retreat more favorable than the progression of a dissolution front along the [010] direction.

In future research, we will use the $(0\bar{4}1)$ terrace-step as a model to investigate forsterite dissolution mechanisms. Specifically, we will carry out Nudged Elastic Band (NEB) and metadynamics calculations to investigate whether forsterite dissolution occurs via a proton promoted or bicarbonate promoted in CO_2 rich water. This work will contribute to a better understanding of CO_2 mineralization processes by carbonation of divalent metal silicates.

Acknowledgments

This work was supported by the U.S. Department of Energy (DOE), Office of Science, Office of Basic Energy Sciences, Chemical Sciences, Geosciences, and Biosciences Division through its Geosciences Program at Pacific Northwest National Laboratory (FWP 56674). Simulations were performed using PNNL Institutional Computing (PIC) resources and the National Energy Research Scientific Computing Center (NERSC), a User Facility supported by the Office of Science of the U.S. DOE under Contract No. DE-AC02-05CH11231. PNNL is a multi-program national laboratory operated by Battelle Memorial Institute under contract no. DE-AC05-76RL01830 for the DOE. We would also like to thank the NWChem and NWChemEx project team and the people who have helped the progress of the NWChem and NWChemEx softwares over the years.

References

(1) Matter, J. M.; Kelemen, P. B. Permanent storage of carbon dioxide in geological reservoirs by mineral carbonation. *Nat. Geosci.* **2009**, *2* (12), 837-841.

(2) Matter, J. M.; Stute, M.; Snæbjörnsdottir, S. Ó.; Oelkers, E. H.; Gislason, S. R.; Aradottir, E. S.; Sigfusson, B.; Gunnarsson, I.; Sigurdardottir, H.; Gunnlaugsson, E.; et al. Rapid carbon mineralization for permanent disposal of anthropogenic carbon dioxide emissions. *Science* **2016**, *352* (6291), 1312.

(3) Snæbjörnsdóttir, S. Ó.; Sigfússon, B.; Marieni, C.; Goldberg, D.; Gislason, S. R.; Oelkers, E. H. Carbon dioxide storage through mineral carbonation. *Nat. Rev. Earth Environ.* **2020**, *1* (2), 90-102.

(4) Kelemen, P.; Benson, S. M.; Pilorgé, H.; Psarras, P.; Wilcox, J. An Overview of the Status and Challenges of CO_2 Storage in Minerals and Geological Formations. *Front. Clim.* **2019**, *1*, Review.

(5) Kerisit, S. N.; Mergelsberg, S. T.; Thompson, C. J.; White, S. K.; Loring, J. S. Thin Water Films Enable Low-Temperature Magnesite Growth Under Conditions Relevant to Geologic Carbon Sequestration. *Environ. Sci. Technol.* **2021**, *55* (18), 12539-12548.

(6) Loring, J. S.; Chen, J.; Bénézeth, P.; Qafoku, O.; Ilton, E. S.; Washton, N. M.; Thompson, C. J.; Martin, P. F.; McGrail, B. P.; Rosso, K. M.; et al. Evidence for Carbonate Surface Complexation during Forsterite Carbonation in Wet Supercritical Carbon Dioxide. *Langmuir* **2015**, *31* (27), 7533-7543.

(7) Mergelsberg, S. T.; Kerisit, S. N.; Ilton, E. S.; Qafoku, O.; Thompson, C. J.; Loring, J. S. Low temperature and limited water activity reveal a pathway to magnesite amorphous magnesium carbonate. *Chem. Commun.* **2020**, *56* (81), 12154-12157.

(8) Mergelsberg, S. T.; Rajan, B. P.; Legg, B. A.; Kovarik, L.; Burton, S. D.; Bowers, G. M.; Bowden, M. E.; Qafoku, O.; Thompson, C. J.; Kerisit, S. N.; et al. Nanoscale Mg-Depleted Layers Slow Carbonation of Forsterite (Mg_2SiO_4) When Water Is Limited. *Environ. Sci. Tech. Lett.* **2023**, *10* (1), 98-104.

(9) Miller, Q. R. S.; Dixon, D. A.; Burton, S. D.; Walter, E. D.; Hoyt, D. W.; McNeill, A. S.; Moon, J. D.; Thanthiriwatte, K. S.; Ilton, E. S.; Qafoku, O.; et al. Surface-Catalyzed Oxygen Exchange during Mineral Carbonation in Nanoscale Water Films. *J. Phys. Chem. C* **2019**, *123* (20), 12871-12885.

(10) Placencia-Gómez, E.; Kerisit, S. N.; Mehta, H. S.; Qafoku, O.; Thompson, C. J.; Graham, T. R.; Ilton, E.; Loring, J. S. Critical Water Coverage during Forsterite Carbonation in Thin Water Films: Activating Dissolution and Mass Transport. *Environ. Sci. Technol.* **2020**, *54* (11), 6888-6899.

(11) Thompson, C. J.; Loring, J. S.; Rosso, K. M.; Wang, Z. M. Comparative reactivity study of forsterite and antigorite in wet supercritical CO by in situ infrared spectroscopy. *Int. J. Greenh. Gas Con.* **2013**, *18*, 246-255.

(12) Thompson, C. J.; Mergelsberg, S. T.; Rajan, B. P.; Martin, P. F.; Kerisit, S. N.; Loring, J. S. Nanoscale control over water-film thickness using temperature modulation: tuning mineral carbonation reactivity. *Environ. Sci. Nano.* **2024**, *11* (4), 1412-1416.

(13) Loring, J. S.; Miller, Q. R. S.; Thompson, C. J.; Schaef, H. T. Chapter 4 - Experimental Studies of Reactivity and Transformations of Rocks and Minerals in Water-Bearing Supercritical CO2. In *Science of Carbon Storage in Deep Saline Formations*, Newell, P., Ilgen, A. G. Eds.; Elsevier, 2019; pp 63-88.

(14) Loring, J. S.; Thompson, C. J.; Wang, Z.; Joly, A. G.; Sklarew, D. S.; Schaef, H. T.; Ilton, E. S.; Rosso, K. M.; Felmy, A. R. In Situ Infrared Spectroscopic Study of Forsterite Carbonation in Wet Supercritical CO2. *Environ. Sci. Technol.* **2011**, *45* (14), 6204-6210.

(15) Loring, J. S.; Webb, T. E.; Bowden, M. E.; Engelhard, M. H.; Kerisit, S. N. Cobalt substitution slows forsterite carbonation in low-water supercritical carbon dioxide. *Phys. Chem. Chem. Phys.* **2024**, 10.1039/D4CP02092H.

(16) Daval, D.; Sissmann, O.; Menguy, N.; Saldi, G. D.; Guyot, F.; Martinez, I.; Corvisier, J.; Garcia, B.; Machouk, I.; Knauss, K. G.; et al. Influence of amorphous silica layer formation on the dissolution rate of olivine at 90°C and elevated pCO2. *Chem. Geol.* **2011**, *284* (1), 193-209.

(17) Olsson, J.; Bovet, N.; Makovicky, E.; Bechgaard, K.; Balogh, Z.; Stipp, S. L. S. Olivine reactivity with CO2 and H2O on a microscale: Implications for carbon sequestration. *Geochim. Cosmochim. Acta* **2012**, *77*, 86-97.

(18) Kerisit, S.; Bylaska, E. J.; Felmy, A. R. Water and carbon dioxide adsorption at olivine surfaces. *Chem. Geol.* **2013**, *359*, 81-89.

(19) Kerisit, S.; Weare, J. H.; Felmy, A. R. Structure and dynamics of forsterite–scCO2/H2O interfaces as a function of water content. *Geochim. Cosmochim. Acta* **2012**, *84*, 137-151.

(20) Zare, S.; Funk, A.; Abdolhosseini Qomi, M. J. Formation and Dissolution of Surface Metal Carbonate Complexes: Implications for Interfacial Carbon Mineralization in Metal Silicates. *J. Phys. Chem. C* **2022**, *126* (28), 11574-11584.

(21) Zare, S.; Uddin, K. M. S.; Funk, A.; Miller, Q. R. S.; Abdolhosseini Qomi, M. J. Nanoconfinement matters in humidified CO2 interaction with metal silicates. *Environ. Sci. Nano* **2022**, *9* (10), 3766-3779, 10.1039/D2EN00148A.

(22) Liu, T.; Gautam, S.; Wang, H.-W.; Anovitz, L. M.; Mamontov, E.; Allard, L. F.; Cole, D. R. Structure and dynamics of water on the forsterite surface. *Phys. Chem. Chem. Phys.* **2018**, *20* (44), 27822-27829, 10.1039/C8CP05075A.

(23) Liu, T.; Gautam, S. S.; Daemen, L. L.; Kolesnikov, A. I.; Anovitz, L. M.; Hartl, M.; Cole, D. R. Vibrational Behavior of Water Adsorbed on Forsterite (Mg_2SiO_4) Surfaces. *ACS Earth Space Chem.* **2020**, *4* (7), 1050-1063.

(24) Liu, T.; Luo, W.; Cole, D. R.; Asthagiri, A. Water adsorption on olivine(010) surfaces: Effect of alkali and transition metal cation doping. *J. Chem. Phys.* **2019**, *150* (4), 044703.

(25) Sun, C.; Yao, Z.; Wang, Q.; Guo, L.; Shen, X. Theoretical study on the organic acid promoted dissolution mechanism of forsterite mineral. *Appl. Surf. Sci.* **2023**, *614*, 156063.

(26) Zamirri, L.; Corno, M.; Rimola, A.; Ugliengo, P. Forsterite Surfaces as Models of Interstellar Core Dust Grains: Computational Study of Carbon Monoxide Adsorption. *ACS Earth Space Chem.* **2017**, *1* (7), 384-398.

(27) Asaduzzaman, A. M.; Laref, S.; Deymier, P. A.; Runge, K.; Cheng, H. P.; Muralidharan, K.; Drake, M. J. A first-principles characterization of water adsorption on forsterite grains. *Philos. Trans. R. Soc. A* **2013**, *371* (1994), 20110582.

(28) de Leeuw, N. H.; Parker, S. C.; Catlow, C. R. A.; Price, G. D. Modelling the effect of water on the surface structure and stability of forsterite. *Phys. Chem. Miner.* **2000**, *27* (5), 332-341.

(29) King, H. E.; Stimpfl, M.; Deymier, P.; Drake, M. J.; Catlow, C. R. A.; Putnis, A.; de Leeuw, N. H. Computer simulations of water interactions with low-coordinated forsterite surface sites: Implications for the origin of water in the inner solar system. *Earth Planet. Sci. Lett.* **2010**, *300* (1), 11-18.

(30) Watson, G. W.; Oliver, P. M.; Parker, S. C. Computer simulation of the structure and stability of forsterite surfaces. *Phys. Chem. Miner.* **1997**, *25* (1), 70-78.

(31) Bruno, M.; Massaro, F. R.; Prencipe, M.; Demichelis, R.; De La Pierre, M.; Nestola, F. Ab Initio Calculations of the Main Crystal Surfaces of Forsterite (Mg_2SiO_4): A Preliminary Study to Understand the Nature of Geochemical Processes at the Olivine Interface. *J. Phys. Chem. C* **2014**, *118* (5), 2498-2506.

(32) Asaduzzaman, A.; Muralidharan, K.; Ganguly, J. Incorporation of water into olivine during nebular condensation: Insights from density functional theory and thermodynamics, and implications for phyllosilicate formation and terrestrial water inventory. *Meteorit. Planet. Sci.* **2015**, *50* (4), 578-589.

(33) Demichelis, R.; Bruno, M.; Massaro, F. R.; Prencipe, M.; De La Pierre, M.; Nestola, F. First-principle modelling of forsterite surface properties: Accuracy of methods and basis sets. *J. Comput. Chem.* **2015**, *36* (19), 1439-1445.

(34) Li, X.; Pedrosa, E. T.; Wang, Q.; Qian, B.; Shen, X.; Lu, D.; Luttge, A. Discontinuous Dissolution Mechanism of Olivine Deduced from a Topography Observation Method. *Langmuir* **2023**, *39* (51), 19008-19015.

(35) Li, X.; Shen, X.; Wang, Q.; Lu, D.; Qian, B.; Pedrosa, E. T.; Luttge, A. Influence of surface orientation on the variability of olivine dissolution rates. *Appl. Surf. Sci.* **2024**, *655*, 159634.

(36) Li, X.; Wang, Q.; Shen, X.; Pedrosa, E. T.; Luttge, A. Multiscale investigation of olivine (010) face dissolution from a surface control perspective. *Appl. Surf. Sci.* **2021**, *549*, 149317.

(37) Becke, A. D. Perspective: Fifty years of density-functional theory in chemical physics. *J. Chem. Phys.* **2014**, *140* (18).

(38) Bylaska, E.; Tsemekhman, K.; Govind, N.; Valiev, M. Large-scale plane-wave-based density functional theory: formalism, parallelization, and applications. *Computational methods for large systems: electronic structure approaches for biotechnology and nanotechnology* **2011**, 77-116.

(39) Apra, E.; Bylaska, E. J.; De Jong, W. A.; Govind, N.; Kowalski, K.; Straatsma, T. P.; Valiev, M.; van Dam, H. J.; Alexeev, Y.; Anchell, J. NWChem: Past, present, and future. *J. Chem. Phys.* **2020**, *152* (18).

(40) Valiev, M.; Bylaska, E. J.; Govind, N.; Kowalski, K.; Straatsma, T. P.; Van Dam, H. J. J.; Wang, D.; Nieplocha, J.; Aprà, E.; Windus, T. L. NWChem: A comprehensive and scalable open-source solution for large scale molecular simulations. *Comput. Phys. Commun.* **2010**, *181* (9), 1477-1489.

(41) Perdew, J. P.; Burke, K.; Ernzerhof, M. Generalized gradient approximation made simple. *Phys. Rev. Lett.* **1996**, *77* (18), 3865.

(42) Hamann, D.; Schlüter, M.; Chiang, C. Norm-conserving pseudopotentials. *Phys. Rev. Lett.* **1979**, *43* (20), 1494.

(43) Hamann, D. R. Generalized norm-conserving pseudopotentials. *Phys. Rev. B* **1989**, *40* (5), 2980.

(44) Troullier, N.; Martins, J. L. Efficient pseudopotentials for plane-wave calculations. *Phys. Rev. B* **1991**, *43* (3), 1993.

(45) Bylander, D.; Kleinman, L. Outer-core—and valence—electron pseudopotential. *Phys. Rev. B* **1984**, *29* (4), 2274.

(46) Dovesi, R.; Civalleri, B.; Roetti, C.; Saunders, V. R.; Orlando, R. Ab initio quantum simulation in solid state chemistry. *Rev. Comput. Chem.* **2005**, *21*, 1-125.

(47) Leadbetter, A.; Ward, R.; Clark, J.; Tucker, P.; Matsuo, T.; Suga, H. The equilibrium low-temperature structure of ice. *J. Chem. Phys.* **1985**, *82* (1), 424-428.

(48) Kristensen, R.; Stipp, S.; Refson, K. Modeling steps and kinks on the surface of calcite. *J. Chem. Phys.* **2004**, *121* (17), 8511-8523.

(49) Bostroem, D. Single-crystal X-ray diffraction studies of synthetic Ni-Mg olivine solid solutions. *Am. Min.* **1987**, *72* (9-10), 965-972.

(50) TobyáKelsey, E.; áde Leeuw, N. H. Atomistic simulation of dislocations, surfaces and interfaces in MgO. *J. Chem. Soc., Faraday Trans.* **1996**, *92* (3), 433-438.

(51) Baker, E. N.; Hubbard, R. E. Hydrogen bonding in globular proteins. *Prog. Biophys. Mol. Bio.* **1984**, *44* (2), 97-179.

(52) de Leeuw, N. H.; Watson, G. W.; Parker, S. C. Atomistic simulation of adsorption of water on three-, four-and five-coordinated surface sites of magnesium oxide. *J. Chem. Soc., Faraday Trans* **1996**, *92* (12), 2081-2091.

(53) de Leeuw, N. H.; Higgins, F. M.; Parker, S. C. Modeling the surface structure and stability of α-quartz. *J. Phys. Chem. B* **1999**, *103* (8), 1270-1277.

(54) de Leeuw, N. H.; Parker, S. C. Surface structure and morphology of calcium carbonate polymorphs calcite, aragonite, and vaterite: an atomistic approach. *J. Phys. Chem. B* **1998**, *102* (16), 2914-2922.

457 **Graphical Table of Contents**

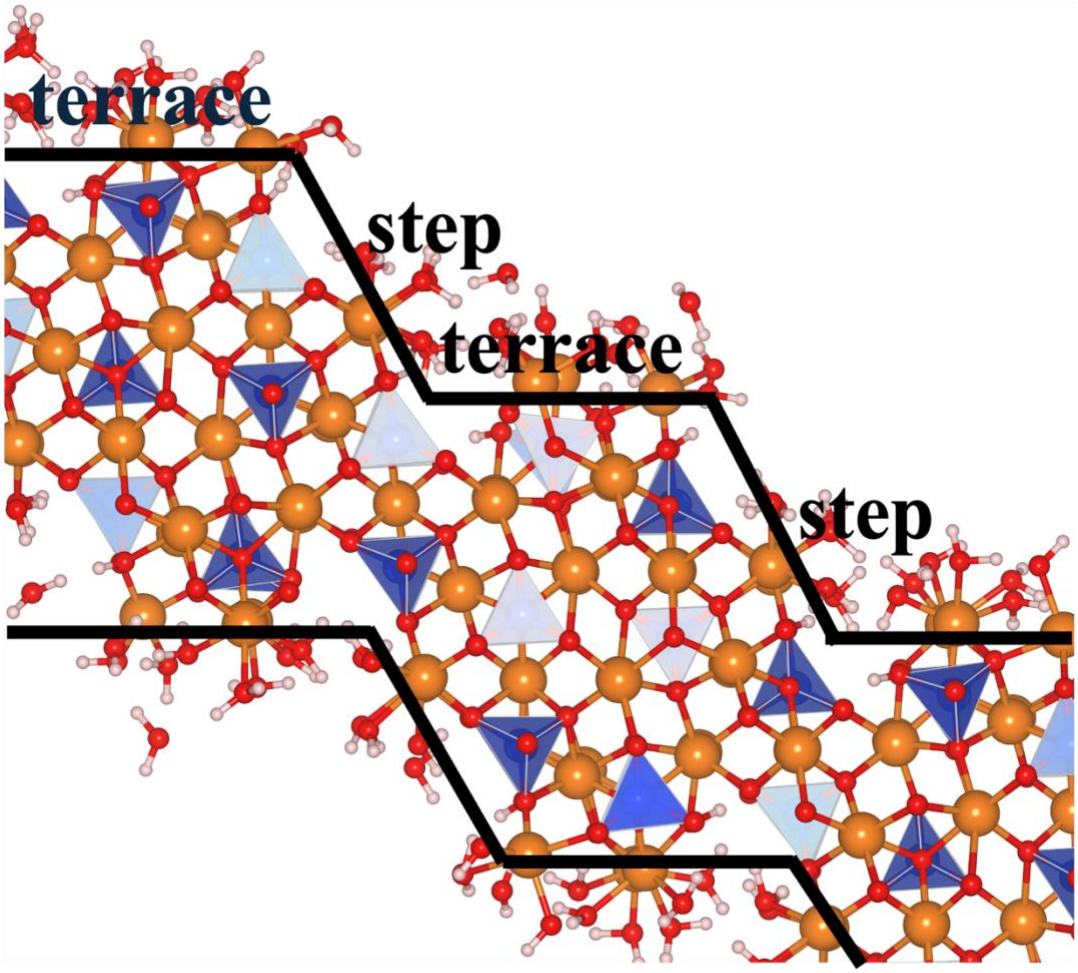

For Table of Contents Only

458